TRMM Precipitation Radar Reflectivity Profiles as Compared with High-Resolution Airborne and Ground-Based Radar Measurements

G. M. HEYMSFIELD

NASA Goddard Space Flight Center, Greenbelt, Maryland

B. GEERTS

Science Systems and Applications, Inc., Lanham, Maryland

L. TIAN

Universities Space Research Associates, Seabrook, Maryland

(Manuscript received 6 October 1999, in final form 1 May 2000)

ABSTRACT

Orbital Tropical Rainfall Measuring Mission (TRMM) precipitation radar (PR) products are evaluated by simultaneous comparisons with high-resolution data from the high-altitude ER-2 Doppler radar (EDOP) and ground-based radars. The purpose is not to calibrate any radar or to validate surface rainfall estimates, but rather to evaluate the vertical reflectivity structure, which is important in TRMM rain-type classification and estimation of latent heating profiles. The radars used in this study have considerably different viewing geometries and resolutions, demanding nontrivial mapping procedures in common earth-relative coordinates. Mapped vertical cross sections and mean profiles of reflectivity from the PR, EDOP, and ground-based radars are compared for six cases. These cases cover a stratiform frontal rainband, convective cells of various sizes and stages, and a hurricane.

For precipitating systems larger than the PR footprint size, PR reflectivity profiles compare very well with high-resolution measurements thresholded to the PR minimum reflectivity, and derived variables such as bright-band height and rain types are accurate, even at off-nadir PR scan angles. Convective rainfall is marked by high-horizontal reflectivity gradients; therefore its reflectivity distribution is spread out because of the PR antenna illumination pattern and by nonuniform beamfilling effects. In these cases, rain-type classification may err and be biased toward the stratiform type, and the average reflectivity tends to be underestimated. The limited sensitivity of the PR implies that large portions of the upper regions of precipitation systems remain undetected. This implication applies to all cases, but the discrepancy is larger for smaller cells for which limited sensitivity is compounded by incomplete beamfilling. These findings have important implications for gridded TRMM products such as monthly mean rainfall.

1. Introduction

The Tropical Rainfall Measuring Mission (TRMM) satellite carries a 13.8-GHz radar, providing real-time and climatological rainfall estimation (Kummerow et al. 1998). Several TRMM field campaigns[1] were held in 1998–99 to validate TRMM radar reflectivity, passive microwave data, and derived estimates of rainfall and latent heating profile. The Texas–Florida Underflight (TEFLUN-A) campaign focused on springtime mesoscale convective systems (MCSs) mainly in southeastern Texas. TEFLUN-B was conducted in August–September 1998 in central Florida, in coordination with the Third Convection and Moisture Experiment (CAMEX-3). The latter focused on hurricanes, especially during their landfall, whereas TEFLUN-B concentrated on central Florida convection, which is largely organized by sea breeze circulations. Last, the TRMM Large-Scale Biosphere–Atmosphere (LBA) interaction in the Amazon took place during the first two months of 1999 in the southwestern quadrant of the Amazon Basin.[2] All experiments were amply supported by sur-

[1] See http://trmm-fc.gsfc.nasa.gov/trmm_gv/field_campaigns/field_campaigns.html.

[2] See experiment plan at http://olympic.atmos.colostate.edu/lba_trmm/.

Corresponding author address: Gerald M. Heymsfield, NASA Goddard Space Flight Center, Code 912, Greenbelt, MD 20771.
E-mail: heymsfield@agnes.gsfc.nasa.gov

face data, in particular a network of rain gauges and radiosondes, a ground-based polarization radar, wind profilers, a cloud physics aircraft penetrating the storms, and a high-altitude aircraft [the National Aeronautics and Space Administration's ER-2 and DC-8 (TEFLUN-B only)] flying over the same storms. Both of these aircraft were equipped with microwave imagers, electric field detectors, and precipitation radars; the ER-2 Doppler radar (EDOP), a dual-antenna (9.6 GHz) X-band radar, is the focus of this paper.

TRMM-coincident aircraft flights over and within precipitating clouds, especially for clouds in the sounding and ground-based radar network, are important to precipitation radar (PR) validation. Coordinated airborne–surface radar measurements provide high spatial and temporal coverage of precipitation systems covered by a single TRMM pass, thereby improving our understanding of how well TRMM measures rainfall from storms of various sizes, intensities, and evolutionary stages. In particular, this high-resolution data can help evaluate the segregation between convective and stratiform precipitation by TRMM-based criteria. The distinction between the convection and stratiform rain is important for rainfall estimation, and also to improve our understanding of the general circulation: the net latent heating associated with stratiform rain in the Tropics tends to occur at a higher level than that associated with convective rain (Johnson and Young 1983; Houze 1989).

A range of quantities are derived from the PR reflectivity profiles. The relative reliability of this information can be assessed only through detailed validation efforts. One approach is to statistically compare TRMM products to independent datasets, such as ground radar, rain gauge, satellite IR, or sounding data. This statistical approach (e.g., Datta et al. 1999) is justified by the sparse sampling nature of the PR, both in space and in time, making simultaneous comparisons too rare. The comparison may be based on distinct precipitation systems, but these ''individual'' differences become insignificant when sufficiently large samples are compared. The availability of a statistically large sample of PR data is questionable in some regions and for some periods. More important, the datasets used in statistical comparisons, in particular rain gauge data, are only indirect measures of the PR measurements, thereby incorporating many uncertainties even when the averages match very well.

Our approach is to compare simultaneous TRMM PR products with high-resolution EDOP and ground-based reflectivity in a small sample of storms. EDOP is a nonscanning instrument with two antennas, one pointing to the nadir, the other pointing 33.5° forward (Heymsfield et al. 1996a). Its vertical and horizontal resolutions are 37.5 and 100 m, respectively. Unlike ground-based radars, its nadir antenna has essentially the same perspective as the PR (Fig. 1). The calibration accuracy of the PR and EDOP are within 1 dB*Z*.

The purpose of this paper is to assess how well the TRMM PR measures the vertical reflectivity structure of a variety of types and sizes of precipitating systems. Comparisons are made between the PR, EDOP, and ground-based radars for six TRMM overpasses during TEFLUN-A and -B, CAMEX-3, and TRMM LBA. The ground-based radars used in this study are the S-band polarization radar (S-POL) radar, the C-band Tropical Ocean and Global Atmosphere (TOGA) radar, and several Weather Surveillance Radar-1988 Doppler (WSR-88D) operational radars. The emphasis of this work is on the comparison of the vertical structures and profiles of EDOP and PR reflectivities, whereas the ground radars provide an independent check on the PR measurements, especially the horizontal structure. Other data, such as passive microwave measurements from the TRMM Microwave Imager (TMI) and the ER-2–based Advanced Microwave Precipitation Radiometer (AMPR; Spencer et al. 1994), are only used in the interpretation of the PR–EDOP comparison. The physical relation between EDOP reflectivity cross sections and upwelling microwave radiances is explained for Florida thunderstorms by Heymsfield et al. (1996b). The PR-derived products, such as brightband (BB) characteristics and precipitation classification, are assessed as well.

Because of the different viewing geometries and resolutions of the various radars, interpolating data to a common coordinate system is required. Section 2 describes the details of the PR and EDOP datasets, differences between them, and the mapping methodology. Section 3 introduces the six examples, including a stratiform frontal rainband; a convective cell in its decaying stage; a small, growing convective cell; a small MCS; and a hurricane (two overflights). Section 4 discusses the vertical structure and mean reflectivity profiles from the radars.

2. Data characteristics and analysis methodology

a. TRMM PR data product definitions

The TRMM PR operational products are described in detail in the National Space Development Agency of Japan (NASDA 1999). Level-1 and -2 products are unmapped data, whereas level-3 data (not used in this paper) provide gridded monthly mean PR-based rainfall estimates for the global Tropics in $5° \times 5°$ boxes. This paper utilizes PR products from 2A21 (path-integrated attenuation and normalized surface backscatter cross section), 2A23 (geolocated reflectivity profile data, presence and height of a radar BB, rain-type classification, and storm-top height), and 2A25 (attenuation-corrected reflectivity and rain-rate profiles). In addition, TMI microwave temperatures (2B11) and visible and infrared scanner (VIRS) infrared temperatures (1B01) are utilized. The process leading from PR level-1 to PR level-2 products includes several operations including quality

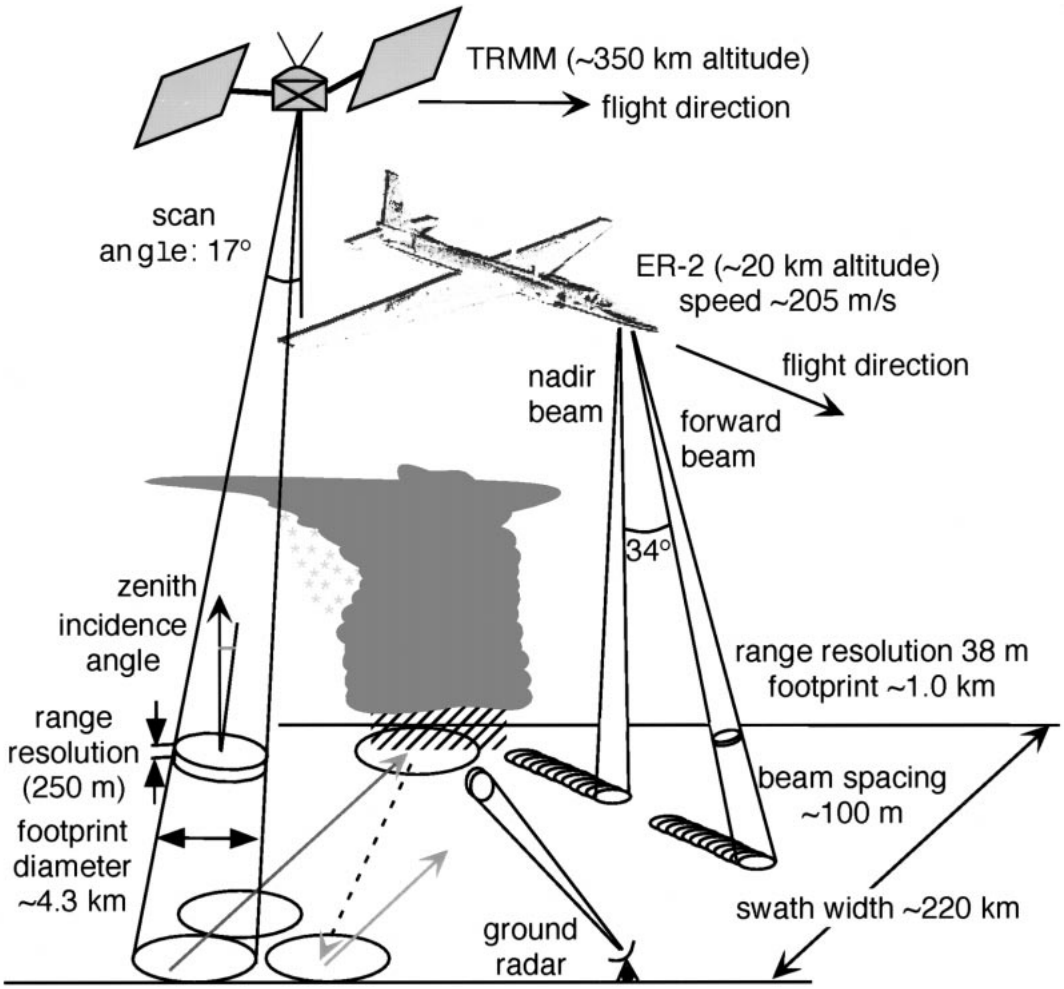

FIG. 1. A comparison of the PR, EDOP, and ground-radar geometries.

control, clutter rejection near the surface, referencing the data to an ellipsoidal representation of the earth's surface, attenuation correction, and a first attempt to correct for nonuniform beamfilling (NUBF). The NUBF correction employed in 2A25 is described in Kozu and Iguchi (1999). A hybrid between the Hitschfeld–Bordan method (Hitschfeld and Bordan 1954) and the surface reference technique (Iguchi and Meneghini 1994) is used to correct for attenuation. The attenuation correction performs well over an ocean background, but worse over land, especially when the precipitation is heavy (Iguchi et al. 2000).

TABLE 1. Definition of TRMM PR rain types as a combination of the outcome of two tests, the H method and the V method. The order of the listing is the same as that in the lower-right corner of Figs. 3–8.

PR rain type	Stratiform	Convective	Inconclusive
Stratiform certain	H, V		
Stratiform certain	V		H
Probably stratiform	H		V
Maybe stratiform	V	H	
Convective certain		H, V	
Convective certain		H	V
Convective certain		V	H
Probably convective		H	V
Maybe convective	H	V	
Maybe convective	V (BB not clear)	H	
Others			H, V

Table 1 summarizes the rain classification scheme used in the 2A23 product. Rainfall is classified as stratiform if a BB exists (''V method'') and/or the horizontal echo variation is small (''H method''). The H method is an adaptation of the method by Steiner et al. (1995) to the PR resolution: a beam is convective if its maximum reflectivity (Z_{max}) exceeds 40 dBZ or if Z_{max} is peaked relative to the ambient echo. In the V method rain is classified as convective if no BB exists and $Z_{max} > 39$ dBZ. Clearly the accuracy of the attenuation correction may significantly affect the rain classification. Both methods yield three outcomes (convective, stratiform, and inconclusive), and a combination of the H and V methods allows rainfall characterization in a

TABLE 2. A comparison of some EDOP and TRMM PR parameters.

	EDOP	TRMM PR
Frequency (GHz)	9.6	13.8
Wavelength (cm)	3.12	2.17
Antenna	Fixed, nadir, and forward (34°)	Scanning to ±17°
Footprint at 5-km altitude (km)	0.76	4.3 (nadir)
Beam spacing (km)	0.1	~4.5
Range resolution (m)	37.5	250*
Time required to sample a 100-km-wide storm (along track)	~8 min	~14 s
Minimum detectable signal (dB*Z*) at 5-km altitude	−5	18
Number of independent samples per pixel	~300	64

* 125 m at incidence angles less than 3.55°.

probabilistic manner. For instance, if both H and V methods classify a pixel as stratiform, the rain type is ''stratiform certain.'' If there is no BB and the H method suggests stratiform rain, then the rain type is ''probably stratiform'' (Table 1). Sample tests indicate that the likelihood of correct BB detection is about 80% near nadir, decreasing to about 20% near the maximum scan angle of 17° (NASDA 1999).

b. EDOP and PR differences

The PR's vantage point, wavelength, and other radar characteristics are significantly different from those of EDOP (Table 2). These differences lead to several important differences in radar observations.

1) Horizontal resolution: EDOP's beamwidth is ~3.0°, which in the nadir translates to ~1.0 km at sea level when the ER-2 flies at 20-km altitude. The PR footprint size is about 4.3 km throughout the troposphere, increasing to about 5.0 km at the maximum incidence angle (17°). EDOP's resolution is sufficient to see shear-induced slopes in hydrometeor fall streaks that are generally undetected by the PR.
2) Sensitivity: The TRMM PR's minimum detectable signal is approximately 18 dB*Z* (e.g., NASDA 1999), which covers all rain rates down to about 0.4 mm h^{-1} (assuming uniform beamfilling). EDOP has a much higher sensitivity (~0 dB*Z* at the surface), allowing it to see the lightest rain and most of the ice region of precipitating clouds. The effects of limited horizontal resolution and low sensitivity combine to exclude isolated, small storm cells from the PR's view. A cell with a diameter of 1 km needs to have an average reflectivity of at least 33 dB*Z* to be seen by the PR (Fig. 4 in Bolen and Chandrasekar 1999). If the cell is located off-center in the PR footprint, the required reflectivity would be even higher, as discussed in appendix B(b).
3) Vertical resolution: The EDOP range resolution is 37.5 m as compared with 250 m in the PR standard products. Therefore the PR *vertical resolution* is 250 m at nadir, decreasing to ~1.6 km (Gaussian weighted) at the outer incidence angle (17°). The PR off-nadir reflectivities are furthermore contaminated by surface clutter for at least part of the lowest 1.6 km at the 17° incidence angle. As a consequence, detailed EDOP-derived BB profiles at nadir can be used to examine the ability of the PR to detect and characterize BBs at varying incidence angles.
4) Attenuation: At 13.8 GHz the PR reflectivity profile suffers from significant attenuation in the lowest levels, both in convective and stratiform precipitation. Attenuation rate (dB km^{-1}) is about ~2.5 times less for EDOP than for the PR. For the PR (EDOP), a 5-km-deep layer of rain with peak reflectivities of ~33 dB*Z* (~39 dB*Z*) results in a two-way path-integrated attenuation (PIA) of ~1 dB. For many situations, EDOP has minimal attenuation for peak reflectivities below ~45 dB*Z*. For intense convective cores, the PR two-way path-integrated attenuation can be significant.

Given these differences, one can treat EDOP cross sections as high-resolution ''truth'' for the TRMM PR. This implies that EDOP data can be ''degraded'' to the PR perspective, and that degraded EDOP data from the various TRMM field campaigns can be used as a surrogate for the PR. This argument was a key motivation for the high-altitude remote sensing aircraft participation in the TRMM field campaigns (Kummerow et al. 2000). TRMM overpasses are relatively rare and do not document the lifecycle of storms, therefore cloud microphysical modeling efforts aimed at improving TRMM precipitation algorithms and derived latent heating profiles will benefit from EDOP data as a complement to TRMM PR data.

Of the four differences listed above, the first one is the most important. Convective precipitation often falls from cells smaller than 4.3 km; in fact, various studies suggest that less than one-quarter of the rain cells have diameters larger than 4.3 km. For example, Goldhirsh and Musiani (1986) found that the median convective cell size near the mid-Atlantic coast of the United States is only 1.9 km. Other studies of tropical precipitation confirm an exponential dropoff in the size distribution of rain cells delineated at various threshold reflectivities (Sauvageot et al. 1999). Therefore, there is valid concern

that NUBF has a systematic effect on PR reflectivity and hence rainfall and latent heating estimates. This concern has been addressed both with theoretical and observed echo patterns (e.g., Nakamura 1991; Amayenc et al. 1996; Testud et al. 1996; Durden et al. 1998); however, real TRMM data have not been used until now. Durden et al. (1998) used a scanning 13.8-GHz radar [the Airborne Rain Mapping Radar (ARMAR)] to simulate PR reflectivities in three dimensions. They found that degraded ARMAR data of tropical oceanic convection tend to overestimate the reflectivity near the cloud tops and underestimate the PIA. Amayenc et al. (1996) also found biases due to NUBF using nadir-looking airborne radar data of a rainstorm off the East Coast of the United States. An attempt is made at the correction of PR rain profile data for NUBF. The approach is a statistical one and assesses the local finescale rainfall variability described by a long record of ground-based radar data (Iguchi et al. 2000). This variability can be correlated with a PR-measurable quantity such as PIA; however, the correlation currently used in the NUBF algorithm is based on radar data in the western equatorial Pacific only (Kozu and Iguchi 1999) and is probably not universally valid. *In short, the de facto impact of subbeam-scale convection and sharp reflectivity gradients on PR rain estimation and classification is not well understood and has not been analyzed by comparing PR data with high-resolution data.*

c. Viewing geometry, resolution, and common frame of reference

Comparison of the PR with EDOP and ground-based radars involves data from drastically different viewing geometries (Fig. 1). Both the PR and EDOP have high vertical resolution but degrade the horizontal structure, while ground-based radars have excellent slant-range resolution but smooth the vertical structure at increasing range. The ground radars themselves, that is, S-POL, TOGA, and WSR-88D radars, have somewhat different range resolutions and beamwidths. Furthermore, the reflectivities from the radars are located at different points in space and time. Comparison of data from these radars requires interpolation to a common reference frame with high-accuracy geolocation. Since TRMM data are widely spaced relative to aircraft and ground-based radar sampling, the choice of interpolation method can be important in filtering and in reducing data aliasing (e.g., Trapp and Doswell 1999). For calibration purposes one would degrade finescale radar measurements to the resolution of the coarsest radar (PR), but the purpose here is to examine finescale reflectivity patterns coincidently observed by the PR, as a way of interpreting the PR reflectivity profile and rain classification. The technique to interpolate the PR and ground-based radars to an EDOP section is described in appendix A. This study uses attenuation-corrected PR reflectivity data (2A25), because the maximum layer-mean reflectivities exceed 35 dBZ in all but one of the cases examined here. EDOP data are not corrected for attenuation because the maximum layer-mean reflectivities are below 45 dBZ in all of the cases. The largest cause of residual difference (i.e., not related to radar characteristics) between correctly geo-interpolated radar data is the nonsimultaneity of the radar measurements. This difference needs to be minimized to address the effect of NUBF and other factors that distinguish PR data from EDOP data. TRMM measurements of a storm are essentially instantaneous, while ground-based radar volumes are collected in 3–5 min and EDOP data are collected in ~8 min $(100\ \text{km})^{-1}$ (appendix B). During a time lag of a few minutes, echo patterns can be displaced significantly (especially in hurricane conditions). They can also evolve such as with small, short-lived convective cells. A better match than the ones presented in this paper could be obtained by correcting the data to a common time, that is, the EDOP observation time. Temporal correction for advection is possible because of the three-dimensional nature of the PR and ground radar data. However, advection vectors cannot be readily estimated, and evolution is the more common culprit of differences in all cases presented in the next section, except the hurricane. Such meteorological differences emphasize the importance of simulating PR data by means of EDOP data, as discussed above. The details of the degrading process are described in appendix B(a). In essence, EDOP data are gridded to a vertical section and then degraded to the TRMM resolution by sampling it with a one-dimensional (along track) representation of the PR antenna illumination function.

3. Synoptic scenario and horizontal radar structure

Figure 2 presents the horizontal radar echo pattern for all six cases. In each case the horizontal precipitation pattern is shown using a TRMM PR 2-km altitude reflectivity map [2A25 constant-altitude plan position indicator (CAPPI)] and a low-elevation PPI scan from the nearest ground radar. Table 2 lists the temporal coincidences of all relevant radars. All the ground-based radars were S-band with 1° beamwidth except the TOGA radar, which is C-band with a 1.6° beamwidth. The horizontal mapping procedures for ground radar and PR data are described in appendixes A(b) and A(c), respectively.

Figures 2a and 2b cover a broad rainband on 21 April 1998 associated with a well-defined WSE–ENE-oriented cold front that slowly propagates southeastward through central Texas. This stratiform rainband is over 700 km long and is aligned with the cold front. The ER-2 flew along this rainband and coincided with the PR swath of the TRMM overpass at 0634 UTC. (All times hereafter are in UTC.) At 0634, there are three short convective lines to the south and west of the ER-2 leg. These lines are oriented normal to the broad rain-

band and move along it, advected by strong westerly wind at 500 mb. They appear more vigorous in the PR image than in the KFWS (Dallas–Fort Worth) radar PPI because the lines are at least 150 km from this WSR-88D radar, therefore their echo strength is reduced by the beam averaging. The ER-2 track began just to the east of the westernmost of these three lines at 0624, and missed the two other lines to the south. By the time of the TRMM overpass about l0 min later, the westernmost line had moved into the ER-2 section.

EDOP data were collected during three TRMM passes over Hurricane Bonnie on 26 August 1998. At the time of the overpasses (1137–1451), Bonnie's central pressure was steady at ~965 mb, and its maximum sustained surface winds were about 50 m s^{-1}. Bonnie made landfall near Wilmington, North Carolina, around 0330 UTC 27 August.[3] At the time of the EDOP observations, Bonnie had one or more weak and ill-defined inner eyewalls and a stronger and more continuous outer eyewall with a diameter of ~170 km. Only the first and third TRMM passes are discussed here. The first TRMM pass at 1137 is over Bonnie's eye (Figs. 2c–d). Several rain arcs can be seen in the region surrounded by the outer eyewall. The PR captures all but the finest features present on the WSR-88D scan, such as the shallow radial bands at the northwestern margin of the storm. By 1450, Bonnie's outer eyewall had contracted slightly and the inner rain arcs had weakened (Figs. 2e–f). While most of the hurricane's rainfall field is north and east of the eye, the outer eyewall is most intense toward the southwest. The PR swath missed the northern part of the outer eyewall on this third pass.

Figures 2g and 2h cover a small MCS with convection embedded in stratiform rain on 23 February 1999, sampled by the ER-2 and S-POL. Between 1900 and 2000 UTC on 23 February, a broken line of cells grew into a continuous line over 100 km long. This line was oriented NNE–SSW and propagated southeastward at first but later stalled. Convection along this line was most vigorous between 2000 and 2030, then weakened and a trailing stratiform region formed to the northwest. By 2200 all convection had disappeared and a ~3,000 km^2 large area of stratiform rain remained. This area expanded and intensified somewhat during the next half-hour, and then dissipated during the next two hours. Easterly winds above 7 km probably supported the formation of the westward-trailing stratiform region. Figures 2g and 2h show this line in a maturing stage. Convection is found mostly to the southeast along the leading line, while the northwestern portion develops into a stratiform region. The EDOP section essentially runs along the leading line of convection. Higher-altitude (6–8 km) PR CAPPIs (not shown) confirm that echoes are strongest to the west of the ER-2 track, while the 2-km CAPPI indicates they are strongest along or just to its east. This is consistent with the observed growth of the stratiform region and has been observed in other squall lines (e.g., Heymsfield et al. 1999).

Figures 2i and 2j are from the trailing edge of a dissipating convective cell on 13 August 1998. In terms of sensitivity, this case illustrates a borderline feature for the PR since there is a significant meridional reflectivity gradient along the zonal EDOP section. The ambient wind was weak at all levels on 13 August, and it was mainly westerly (<8 m s^{-1}) below 10 km. Afternoon thunderstorms developed, mainly along outflow, sea breeze and river breeze boundaries. About 15 km inland from the Banana River, a sequence of short-lived thunderstorms propagated discretely southward and dissipated on the northern side. The ER-2 flew from west to east across the northern edge of one these storms.

On 1 February 1999 in Rondonia, Brazil, many convective towers formed in the TRMM network, but they were generally small and short-lived. At the time of the TRMM overpass, the ER-2 flew near the western edge of a line of convective cells, about 40 km long and 5–10 km wide. This line is captured both by the S-POL PPI and the PR CAPPI in Figs. 2k and 2l. TRMM detected minimal echo from this cell, whereas S-POL observed a weak cell. During this flight, EDOP recorded 12 cells with at least 40 dB*Z* at an altitude of 2 km during the 3-h flight duration over the network (1730–2030). The average diameter of these cells was 5 km (i.e., about the size of the PR footprint) with the exception of a 30-km-wide storm overflown twice. The sample is somewhat biased because the ER-2 targeted the larger thunderstorms in the population. The tops of these storms varied from 5 to 9 km, and no spreading anvils nor stratiform regions formed.

4. Vertical reflectivity structure and relation to other TRMM measurements

a. Reflectivity cross sections, rain classification, and microwave signatures

Figures 3–8 show the vertical reflectivity structure observed by EDOP, ground-based radar, and the TRMM PR. The reflectivity from the different radars are mapped (see appendix A) onto the same Cartesian (x, z) grid above ground level. These figures also show other TRMM products: the brightness temperatures (10–85 GHz and 11 μm) from the TMI and VIRS, respectively; storm-top and BB heights; and PR incidence angle together with rain type. These figures will be discussed in the subsequent sections. The PR storm-top height (2A25 product), that is, the height of the first (highest) echo above the PR noise level, will be compared to the EDOP-estimated storm top.

[3] See the preliminary report by NHC at http://www.nhc.noaa.gov/1998bonnie.html.

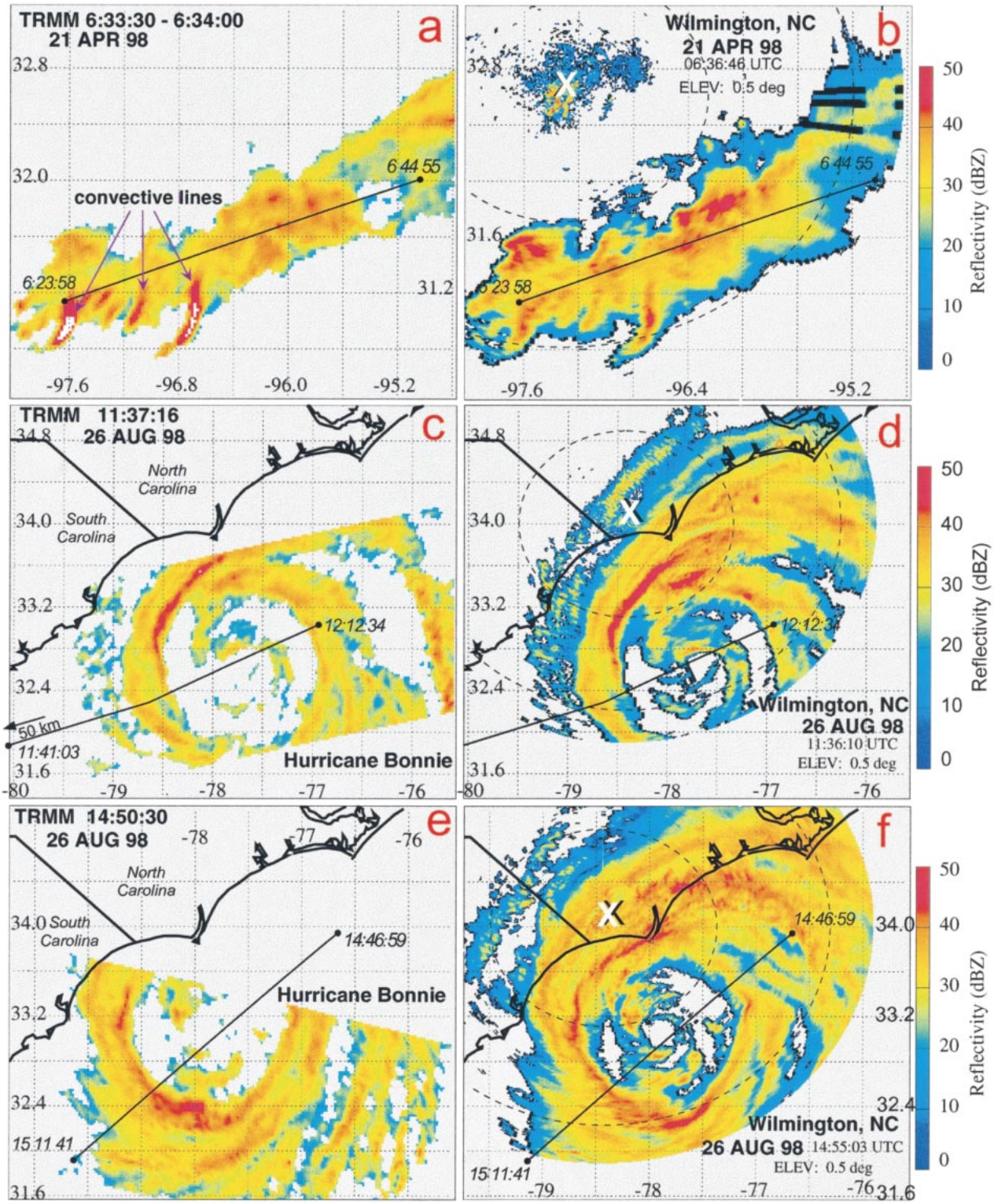

FIG. 2. Reflectivities from TRMM PR and ground-based radar mapped to common earth coordinates. Panels (a), (c), (e), (g), (i) and (k) show the PR reflectivity at 2-km altitude. Panels (b), (d), (f), (h), (j), and (l) display the lowest clutter-free radar elevation scan from the various ground radars. The ER-2 flight track along with start and end times (UTC) is indicated on the plot. Values exceeding 50 dBZ are shown as white, values less than 0 dBZ are black, and the background is gray. The ''×'' denotes the location of the relevant ground radar; the 100- and 200-km-range circles are dashed.

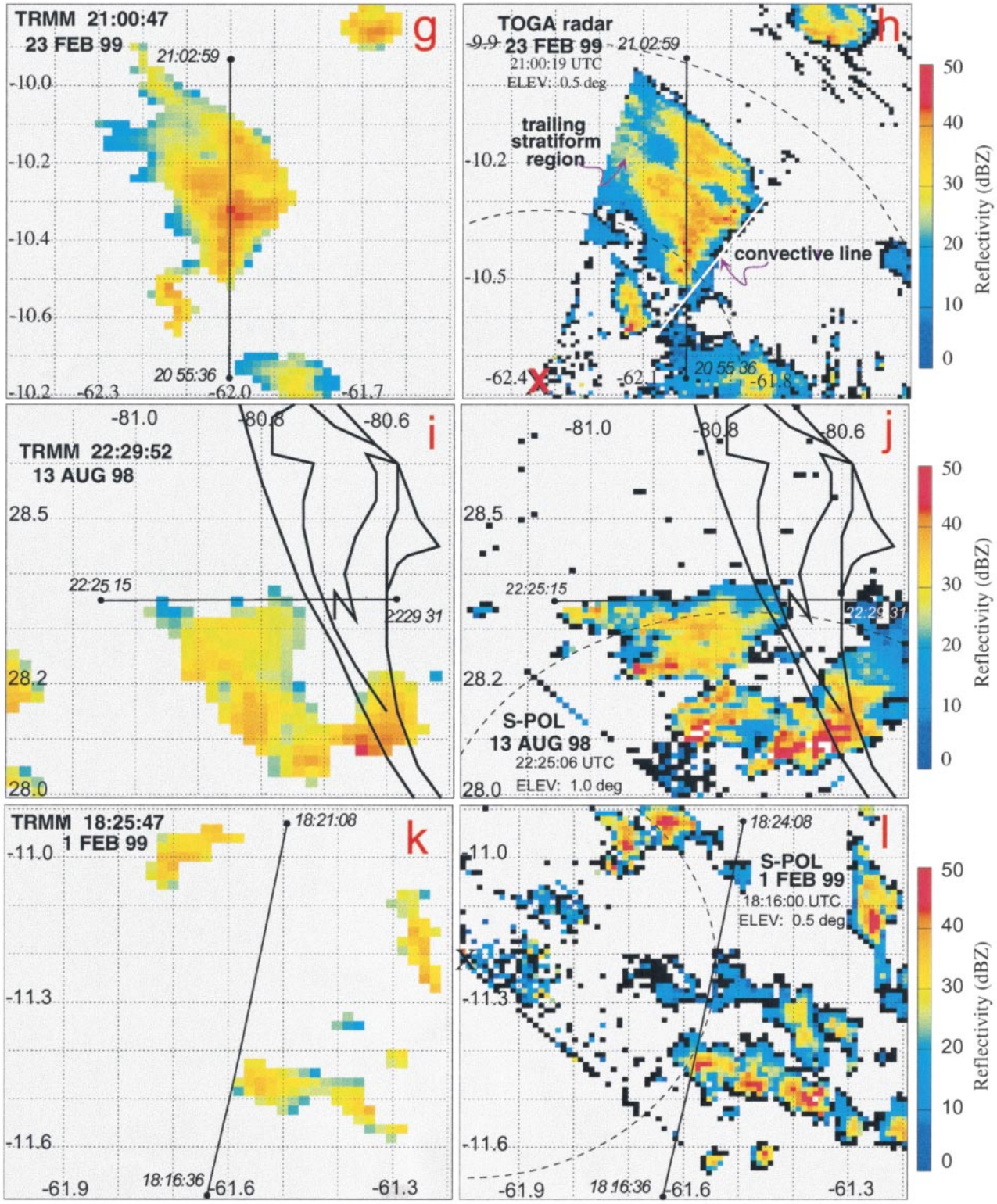

FIG. 2. (*Continued*) Same as previous except range circles are 50 km (h), (j), (l) and 100 km (h).

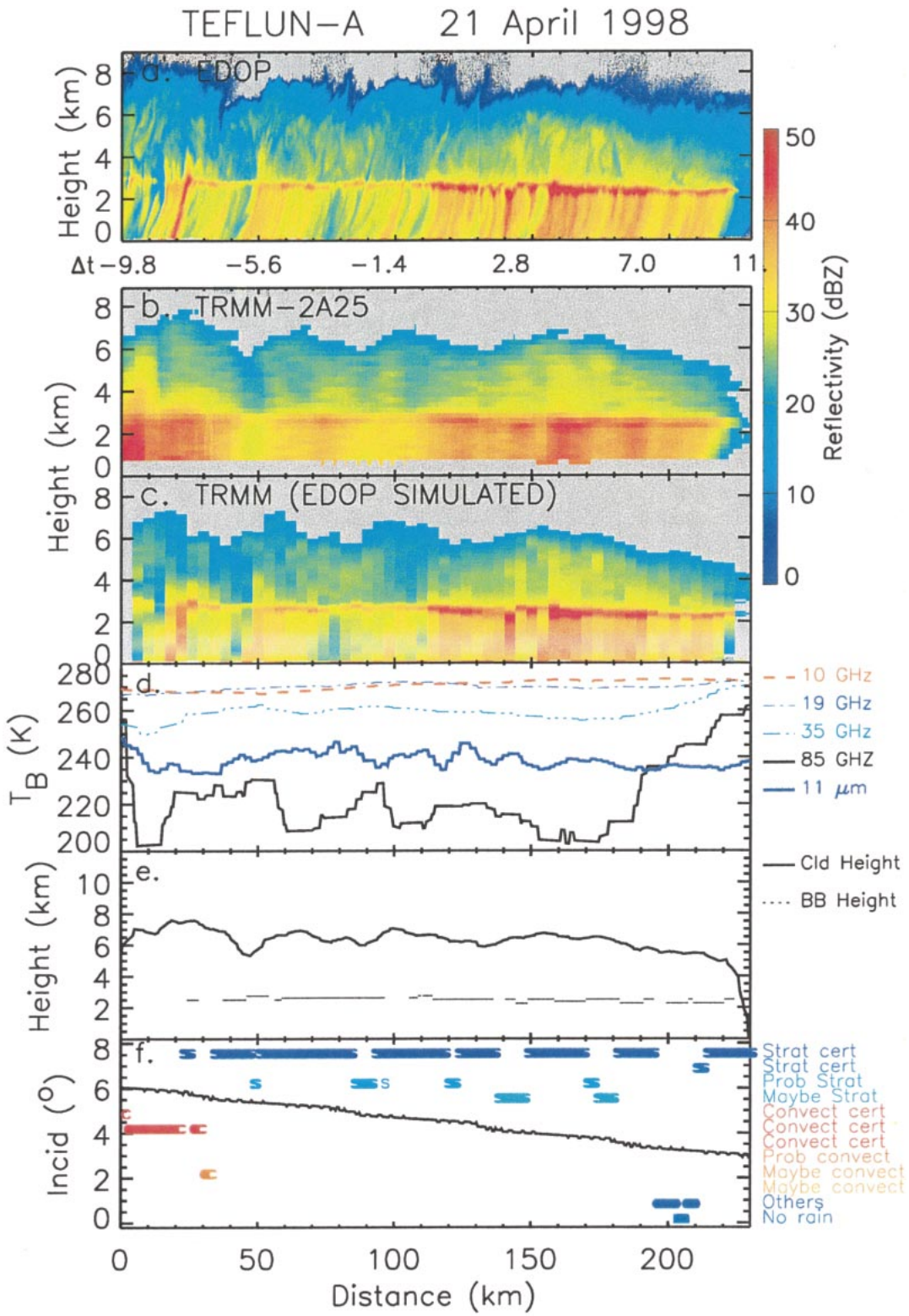

FIG. 3. Composite of vertical reflectivity sections from (a) EDOP and (b) the PR, for 21 Apr 1998, mapped to coordinates of EDOP cross section (top). (c) A degraded EDOP section is shown, simulating the PR (appendix B). The time difference (Δt, min) between the EDOP profile and the PR overpass is labeled below the EDOP image, where positive numbers indicate that the EDOP profile is later than the TRMM image. (d)–(f) show various TRMM products corresponding to this cross section. TMI microwave brightness temperatures at 10, 19, 35, and 85.5 GHz, together with the VIRS infrared brightness temperature, are shown in (d). PR-derived storm top and BB heights are shown in (e), and the rain-type classification (Table 3) is shown in (f) together with the PR incidence angle.

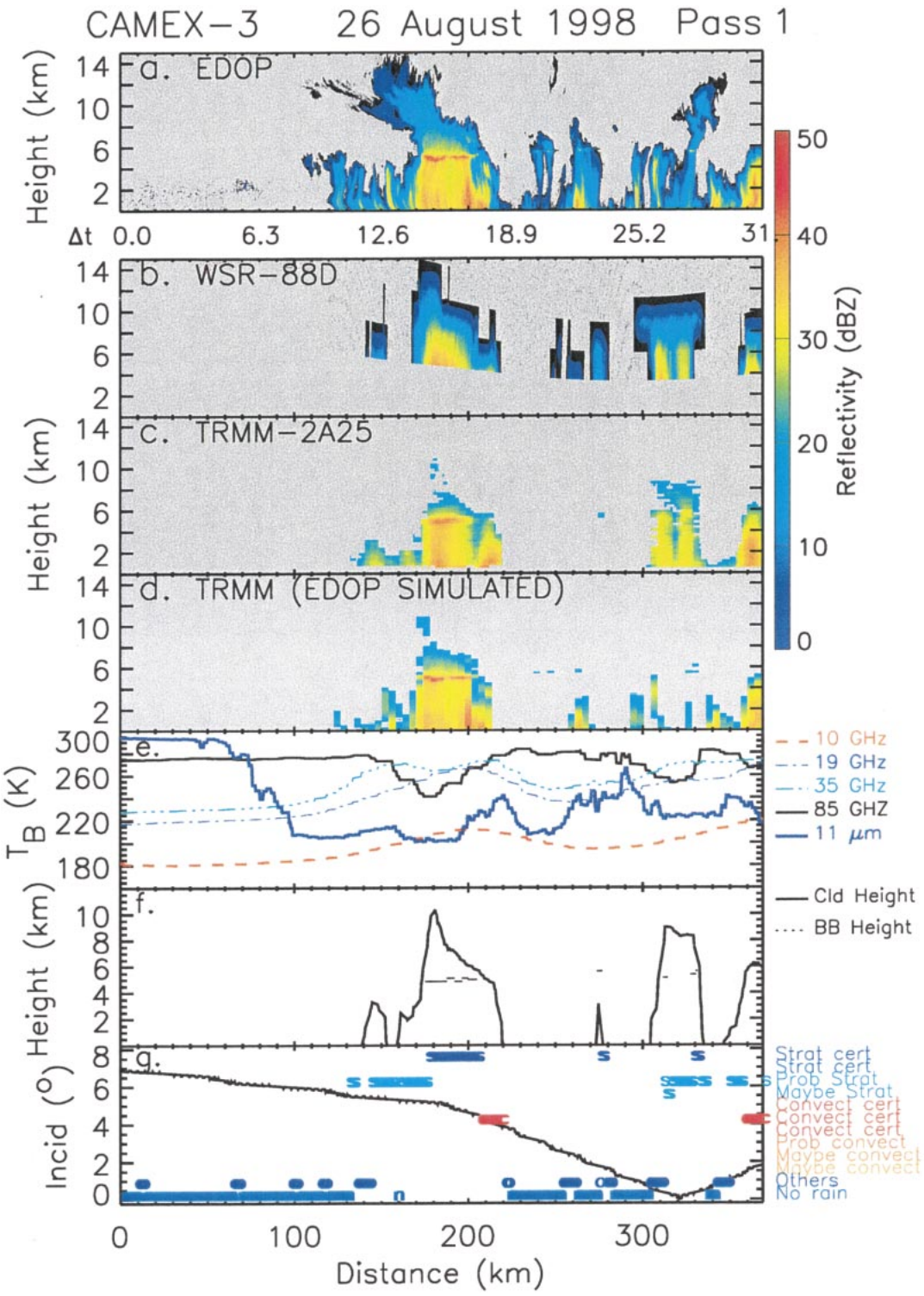

FIG. 4. Same as Fig. 3, but for 26 Aug 1998 (pass 1).

1) WIDESPREAD STRATIFORM RAIN (21 APRIL 1998)

The PR reflectivity pattern matches EDOP's very well for the eastern half of this line, as PR-EDOP coincidence improves to the east (Fig. 3a). Some details are missed by the PR, such as the sloping precipitation fall streaks observed by EDOP below the freezing level. In general, the storm-top height from the PR (Fig. 3b) is about 1

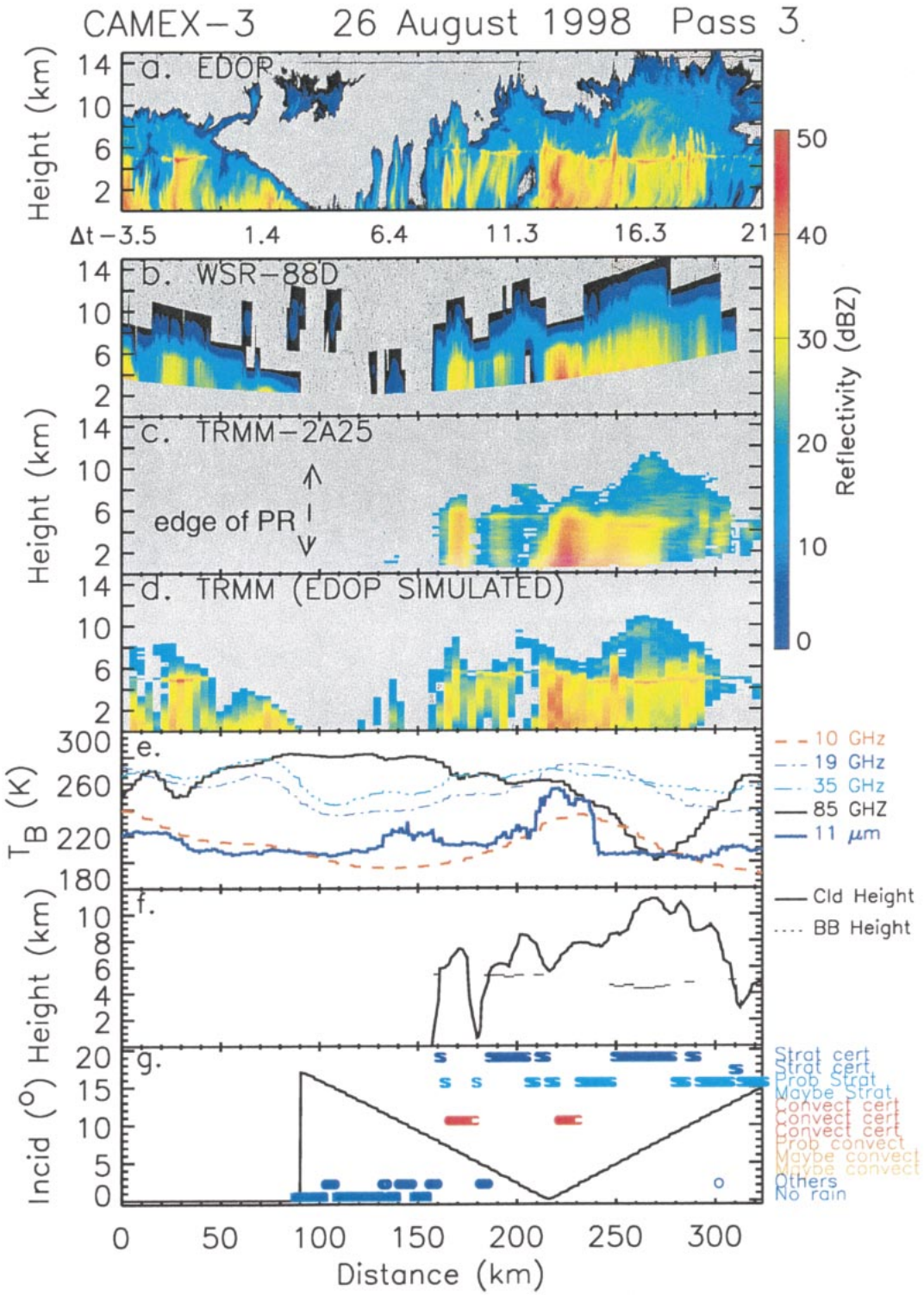

FIG. 5. Same as Fig. 3, but for 26 Aug 1998 (pass 3).

km lower than the EDOP storm top and the EDOP storm top is close to the VIRS 11-μm cloud top of ~235 K (7.5–8.5 km) in Fig. 3d. This suggests that the depth between the 18-dBZ level and the actual cloud top is rather small. The BB height from the PR (Fig. 3e) agrees with EDOP, and the rain east of the convective line (at the left edge of Fig. 3) is classified correctly in the stratiform group. In comparison with tropical stratiform

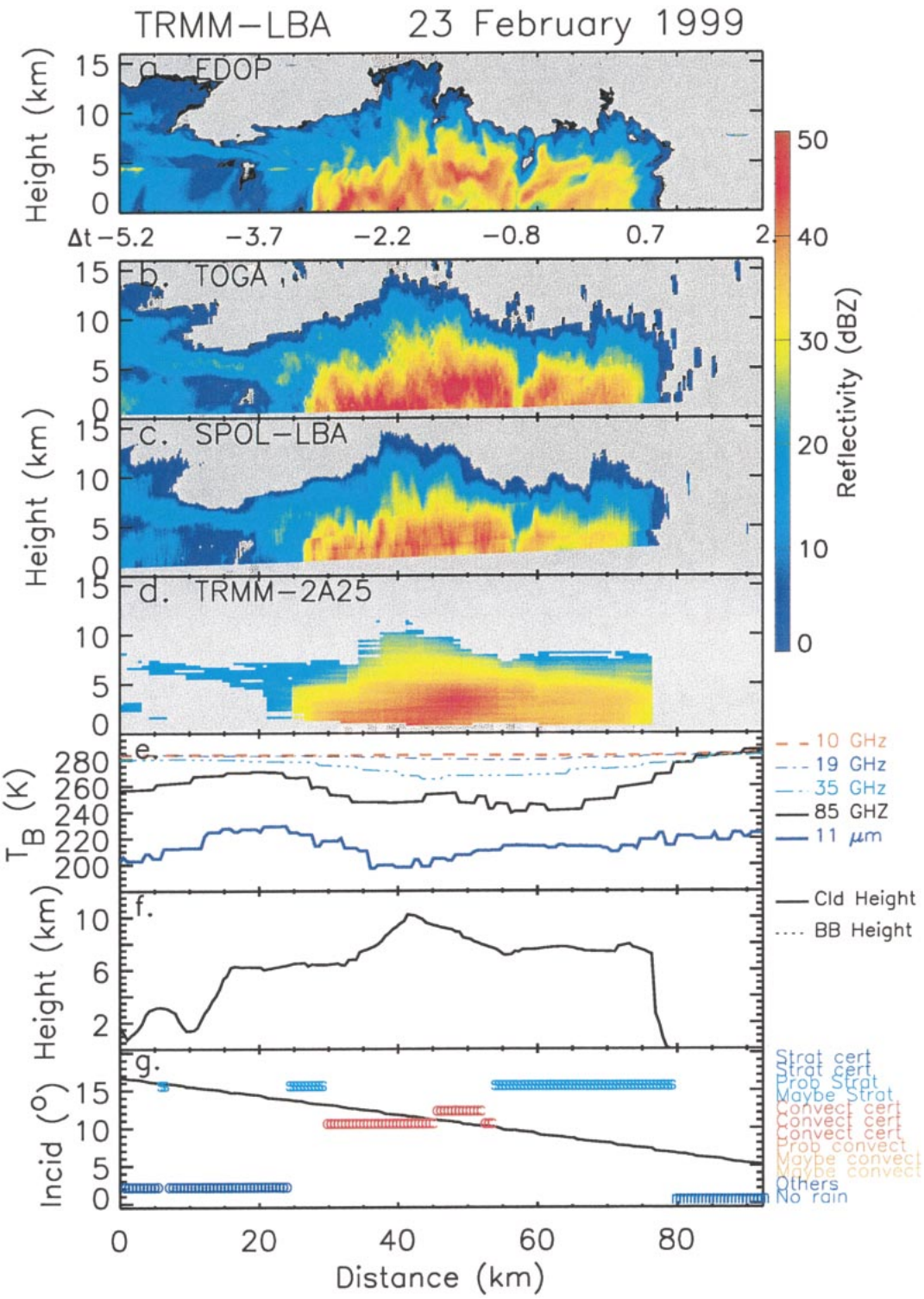

FIG. 6. Same as Fig. 3, but for 23 Feb 1999. The TRMM simulation by means of EDOP data is omitted; instead a reflectivity cross section from a second ground radar is shown.

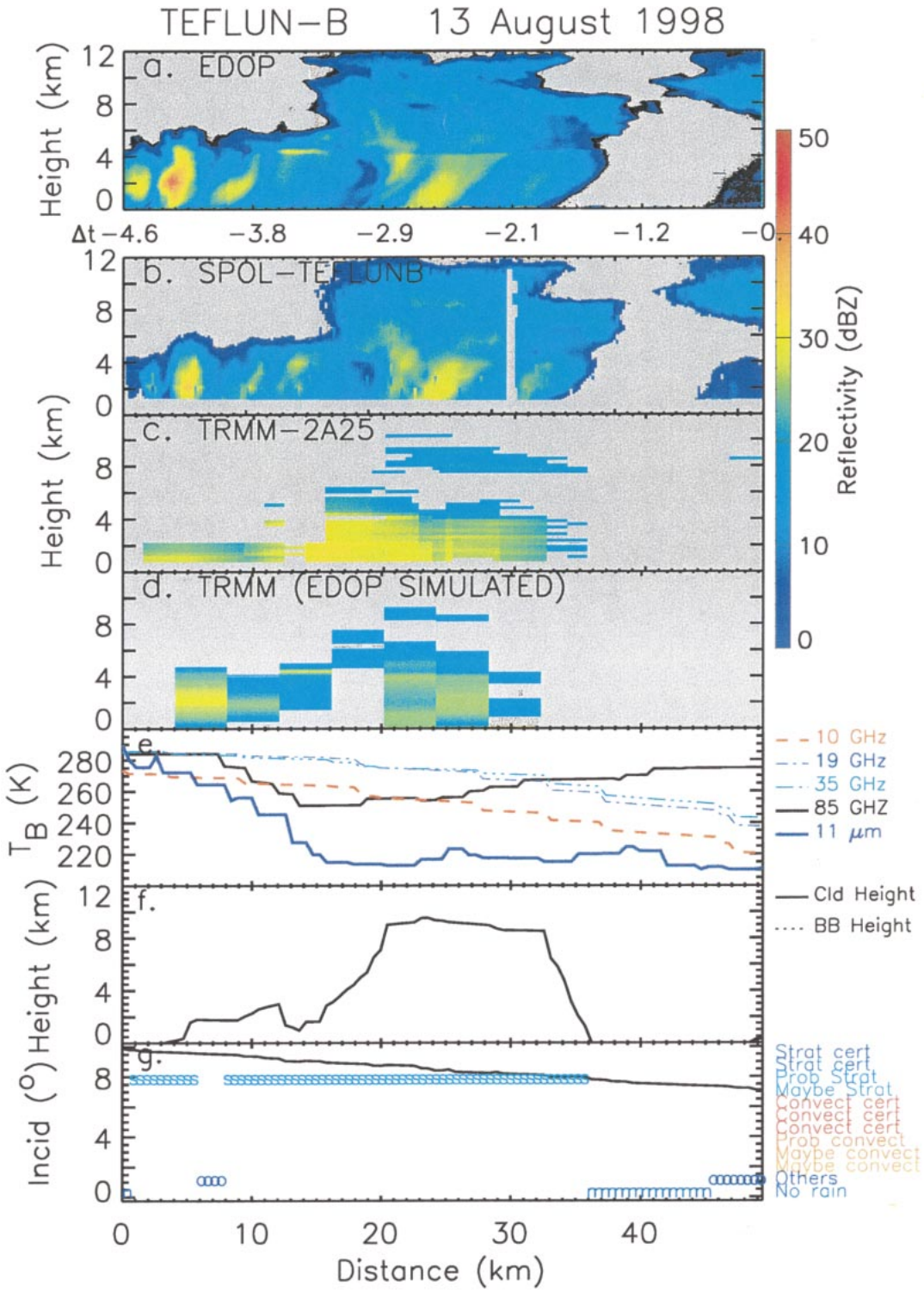

FIG. 7. Same as Fig. 3, but for 13 Aug 1998.

rainfall systems (e.g., in hurricanes, shown later in Figs. 4 and 5), this rainband contains large ice-scattering aloft, as shown by the 85-GHz temperature trace (Fig. 3d). This is not because of high cloud tops (~8 km) but because of the lower freezing level (~2.7-km altitude) in the Tropics. Over much of the rainband the 85-GHz brightness temperature measured by the TMI and AMPR is below 220 K. McGaughey et al. (1996) find that 220

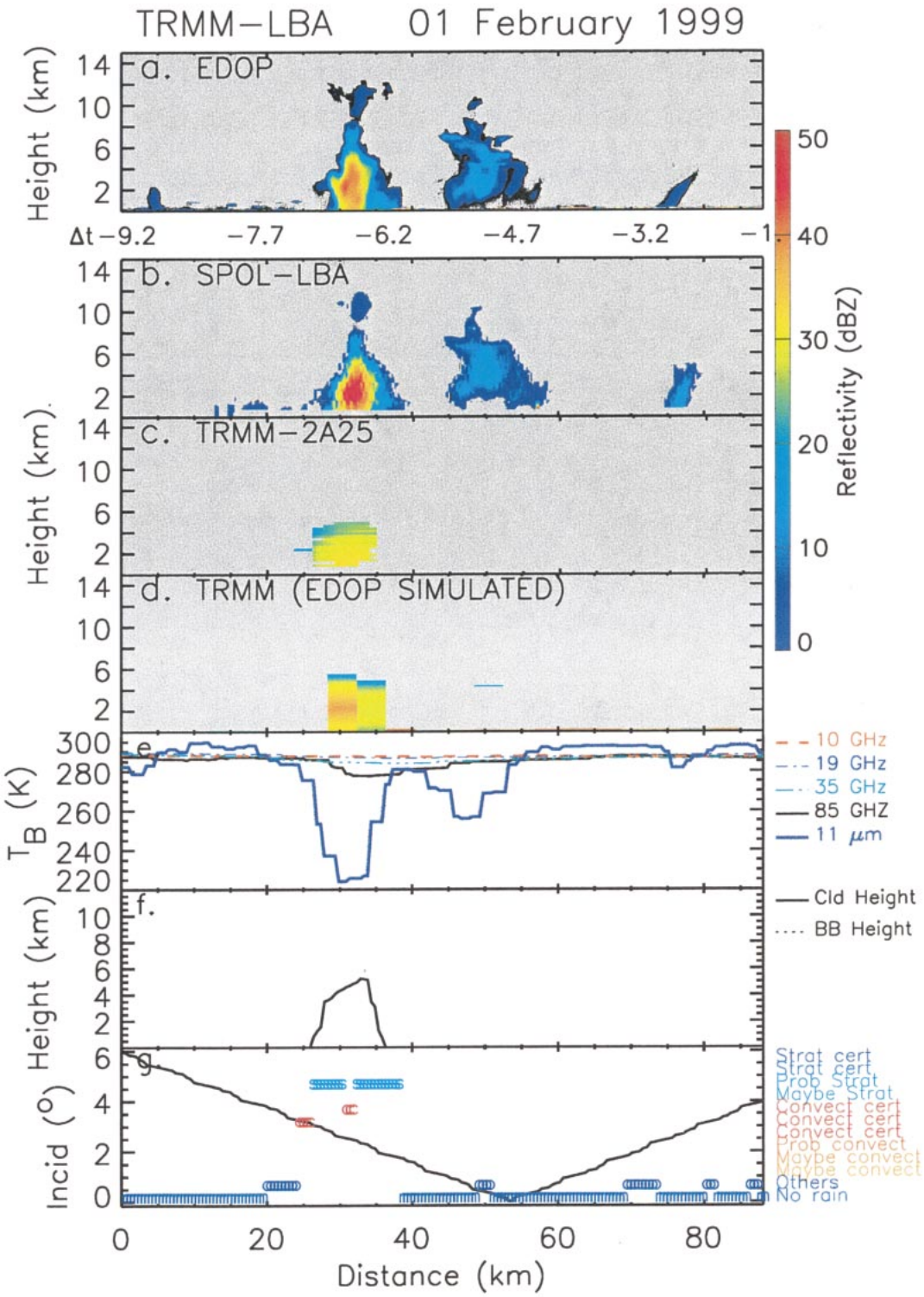

FIG. 8. Same as Fig. 3, but for 1 Feb 1999.

K is the minimum 85-GHz brightness temperature associated with ice scattering in stratiform regions of tropical oceanic systems. Passive microwave temperatures from lower frequencies (especially 19 and 10 GHz) are only marginally depressed (Fig. 3d), because surface emission masks the rain.

2) HURRICANE BONNIE (26 AUGUST 1998)

The EDOP section for pass 1 (Fig. 4a) depicts an asymmetric hurricane, with a highly tilted yet weak northeast eyewall, a deeper southwest eyewall, and with the eye centered near $x = 150$ km. The EDOP section displays finescale features beyond the resolution or sensitivity of the PR (Fig. 4c). For example, many shallow but intense echoes are present within the EDOP-measured outer eyewall ($x = 120$–180 km). The EDOP section lags the TRMM section by 13–35 min, which may account for some of the differences between the PR (Fig. 4c) and the corresponding degraded EDOP section (Fig. 4d). The PR storm tops (Fig. 4f) of the deeper features are 2–4 km lower than EDOP heights, with significant portions of the ice region missing. In this case, the PR algorithms correctly detect and place the BB, even at high incidence angles. Most rain is correctly classified as ''certainly stratiform'' or probably stratiform (Fig. 4g).

The lowest TMI 85-GHz brightness temperature associated with the outer eyewall (near $x = 190$ km) is only 240 K (compared to 220 K for AMPR), rather warm compared to continental convection, suggesting an absence of significant ice scattering. This observation is also corroborated by the low reflectivities aloft. This is common for tropical oceanic MCSs (McGaughey et al. 1996). Most of the inner eyewall remains undetected at 85 GHz, in the passive measurements (TMI and AMPR), implying that ice hydrometeors are small above the freezing level.

For pass 3 (Fig. 5), EDOP and PR reflectivities compare well. The reflectivity from the PR section shows a deep cell ($x = 170$ km, Fig. 5c) and when the ER-2 flies overhead about 10 min later, this cell has largely been advected out of the cross section; therefore the degraded EDOP echo is weaker than the PR echo. The PR BB height (Fig. 5f is similar to EDOP's except that the latter height is elevated due to a higher 0°C isotherm within the eyewall. The cloud height in the outer eyewall ($x = 170$–200 km) derived from the PR is significantly (2–4 km) below the EDOP and actual cloud height because of the limitations on PR sensitivity as in previous cases. Some fall streaks below 5-km altitude (120 km $< x <$ 150 km) with a maximum reflectivity of ~25 dB are too thin and/or too weak to be seen, so no PR cloud height was assigned.

Overall, a BB is detected correctly by the PR algorithm. The rainfall classification scheme is excellent, even at high incidence angles. Areas classified certainly stratiform ($x = 170$–190 km) appear clearly as stratiform in EDOP imagery, and for the two areas classified as convective, EDOP does not reveal a BB. The 85-GHz temperatures measured by the TMI (Fig. 5e) are depressed by the shallow cells inside of the outer eyewall and are as low as 205 K over the southwestern outer eyewall, corresponding well with AMPR (not shown).

3) SMALL MCS (23 FEBRUARY 1999)

No BB is present in this case (Fig. 6a), except for $x < 20$ km where remnants of the shorter-lived southern portion of the line produce a weak BB. Except for an active cell ($x \sim 42$ km) with a cloud top near 15 km, the remaining precipitation is mostly convective remnants. The ground-based radars (Figs. 6b,c), especially TOGA that is closer to the cell, agree with the EDOP echo pattern well. The height, intensity, and structure of the PR echo also compares well to the degraded EDOP echo pattern (not shown), because the EDOP-PR sampling time difference is less than 3 min in the precipitation region. The small discrepancies are mainly due to advection of precipitation and precipitation development into and out of the section. TMI and AMPR images (not shown) indicate that ice aloft is transported to the west of the line (i.e., into the page of Fig. 6a). Minimum 85-GHz temperatures along the ER-2 flight track are quite different between the TMI (~240 K in Fig. 6e) and AMPR (~160 K), presumably due to resolution differences.

The PR rainfall is classified as ''certainly convective'' to the south and probably stratiform to the north (Fig. 6g). The classification as stratiform is not due to a BB (neither the PR nor EDOP detect a BB), but to weak reflectivities. This northern (right hand) region appears convective from an EDOP perspective, because of high reflectivities and an absence of a BB. The PR storm-top height (Fig. 6f) in the precipitation region is several kilometers lower than that of the other radars (EDOP, TOGA, and S-POL in Figs. 6a–c), except to the south ($x < 15$ km) where stratiform and dissipating clouds have higher tops in the 2A23 storm-top product.

4) TRAILING EDGE OF A DISSIPATING CONVECTIVE CELL (13 AUGUST 1998)

The EDOP reflectivity is low at all levels (Fig. 7a) and shows a weak BB. The PR covers this storm from 1 min (right-hand side Fig. 7a) to 4 min (left-hand side) later and detects the storm cell along with some of its decaying anvil (Fig. 7c). The PR storm top (just below 10 km) is about 2 km below the EDOP storm top (Fig. 7f), and rain reaches the ground shown by all radars. The PR classified this rain region as probably stratiform based on the H method since the echo is weak (see Table 1). A BB was not detected since it was thin and weak and because the PR incidence angle is fairly large (8°). Clearly all this precipitation was of convective origin,

and there was no evidence of mesoscale ascent responsible for the formation and maintenance of a stratiform region. Anvil debris resulting from rapidly decaying convection should be labeled as convective even if a BB is detected (Biggerstaff and Listemaa 2000).

The PR only marginally detects the smaller, but more intense, shallow cells to the west ($x < 10$ km in Fig. 7), about 4 min after the ER-2 passage. The TMI 85-GHz temperatures at 10 and 19 GHz (Fig. 7e) are lower than at 85 GHz for these cells, suggesting low ice contents. The cells are not detected by the PR. This detection failure may be affected by NUBF; however, the degraded EDOP image (Fig. 7d) suggests that the PR should still capture a clear signal. The more likely cause is the rapid decay of these shallow, isolated cells. In the 2225 S-POL volume, shown in Figs. 2i and 7b, these cells are much stronger than in the 2231 volume (not shown). Another factor may be the across-leg reflectivity gradient (i.e., normal to the cross section) apparent in Fig. 2i.

5) SMALL CONVECTIVE CELL (1 FEBRUARY 1999)

The line is moving southward and growing in length, but the cell at $x = 35$ km in Fig. 8a (visited twice by EDOP) is dissipating. Yet, it still has a narrow intense core with very few hydrometeors above 5 km and no anvil. The S-POL section (Fig. 8b) is almost identical to EDOP's, but with lower vertical resolution. The PR detects this cell ~6.6 min later, located close to TRMM nadir (Fig. 8c). However, the maximum reflectivity and storm top are ~30 dB*Z* and 5 km, respectively, as compared with 45 dB*Z* and 12 km in EDOP and S-POL data. The degraded EDOP (Fig. 8d) shows a stronger and slightly deeper echo pattern than the PR. The difference may be partly explained by cell evolution. It also depends on the cell location relative to the PR antenna illumination function [appendix B(b)]. When the ER-2 returned along the same path ~6.8 min after the TRMM passage (not shown), the maximum reflectivity had dropped to about 38 dB*Z* and the echo top decreased to about 10 km. The minimum AMPR 8.5-GHz brightness temperature from this cell was about 240 K (not shown), but the TMI 85-GHz temperature traces hardly indicated any disturbance (Fig. 8e). On the other hand, the VIRS temperatures of just below 225 K indicate the cell clearly. The main cell is classified as ''other'' and probably stratiform because of low PR maximum reflectivities (Table 1). The size and strength of this feature, as revealed in EDOP imagery, makes it clearly convective. Only in the core of this cell, a few PR pixels indicate ''convection certain'' (Fig. 8g). In other words, the 2A23 algorithm places an artificial fringe of stratiform rain around the convection.

The weak, dissipating cell to the north of the main cell along this flight leg near $x = 50$ km (Fig. 8a) appears too weak to be seen by the PR. The PR simulation from the EDOP image (Fig. 8d) marginally detects this cell. But, the ER-2 return flight along this leg and S-POL imagery suggests gradual dissipation. Again, only VIRS (Fig. 8e) measurements of this weak feature detected the cell. This weak cell contributes insignificantly to the total rainfall, but such cells are widespread in Brazil and they remain largely undetected.

b. Comparison of mean vertical profiles

Mean height profiles of reflectivity were constructed (Fig. 9) for the cross sections shown in Figs. 3–8. These profiles were obtained by first converting reflectivities in ''dB*Z*'' to linear units before averaging across each height level (37.5 m for EDOP and ground-based radars and 250-m intervals for the PR). Reflectivity profiles from radars other than the PR are thresholded to the PR's minimum detectable reflectivity of 18 dB*Z* so the same precipitation structures are compared. Mean profiles for ground-based radars were truncated near the ground because the upward slanting of the lowest beam away from the radar caused a bias in the averaging length at a particular level. The same truncation was necessary for PR data sampled from low- to high-incidence angles. Much information is lost in the reduction of a precipitating system to a mean profile, but the comparison of the first moment only from various radars is more feasible than that of the contoured frequency by altitude diagrams (Yuter and Houze 1995) or other distribution functions. The mean profiles are also useful for calibration purposes, but the focus in this study is on the details of the profiles. For instance, how does the thickness and the strength of the BB in the PR compare to that of EDOP and that of ground radars? How does reflectivity change with height below the BB, and what cloud microphysical consequences can be drawn? How do profiles compare in the case of NUBF?

The vertical filtering due to the PR's gate spacing and off-nadir viewing results in an underestimation of the BB strength of 2–4 dB*Z* (Figs. 9a and 9b). The PR BB height matches that of EDOP very well, although EDOP often observes BB thicknesses much less than the 250-m PR range gate spacing. Although, it should be cautioned that the BB thickness for both the PR and EDOP is likely overestimated due to the extensive region over which averaging is performed. In both the frontal rainband (Fig. 9a) and Hurricane Bonnie (Fig. 9b), slight variations of the height of the freezing level occur along the EDOP flight leg.

The effect of NUBF is illustrated well in the profiles. The cell in Fig. 9f is small relative to the PR footprint. The PR estimate covering this line is 4–10 dB*Z* lower than that of EDOP and S-POL, and the reflectivity-based cloud top is also much lower. The reason for this is explained in appendix B(b). Not only is the size of the cell relative to the PR footprint important, but also the location of the cell within the footprint affects the reflectivity estimate. *For a given subbeam-scale cell, the reflectivity will be higher at nadir than off-nadir.* An-

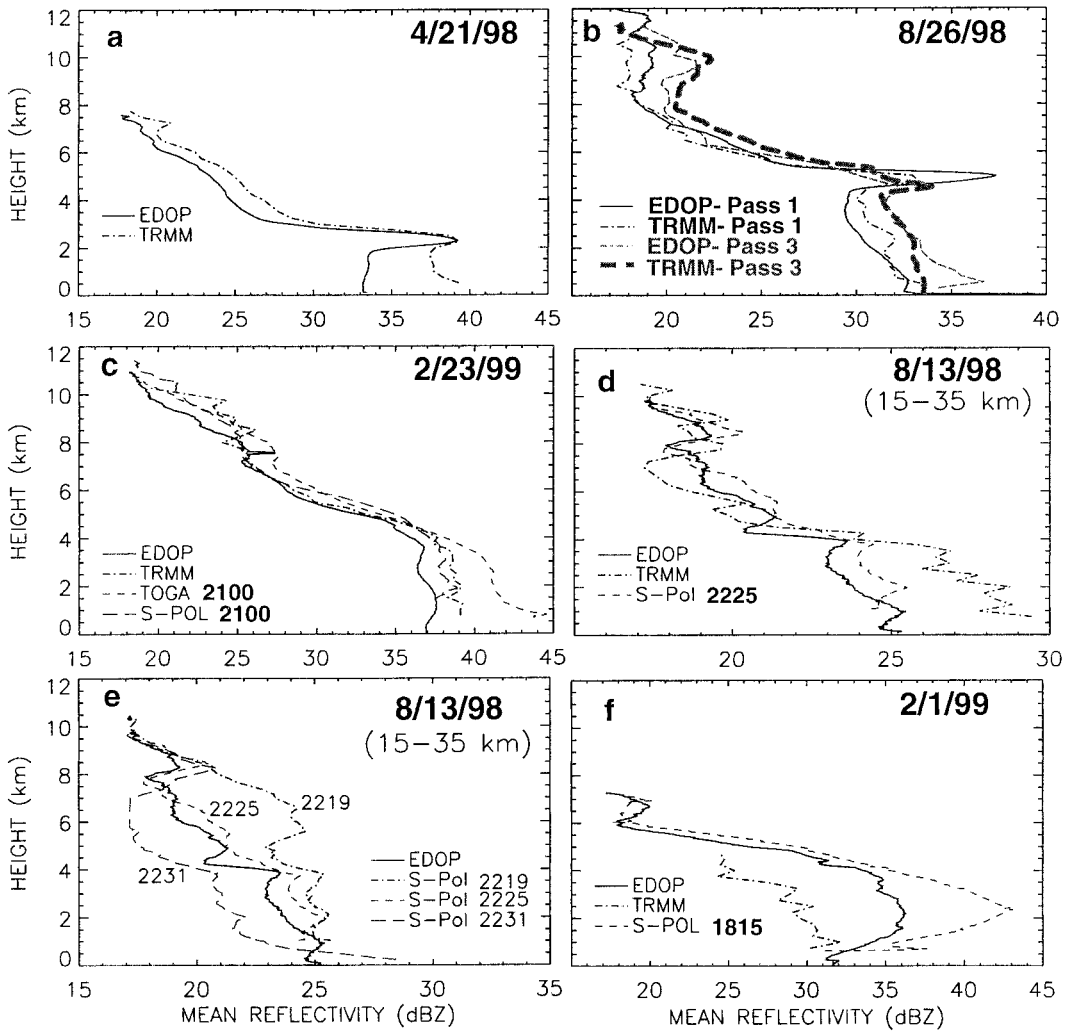

FIG. 9. Mean reflectivity profiles derived from the vertical cross sections in Figs. 3–8. The averages are calculated over the entire section, except where shown (i.e., for 13 Aug). Ground-radar profiles are identified also by the start time of the volume scans. (a) 21 Apr 1998, (b) 26 Aug 1998, (c) 23 Feb 1999, (d) 13 Aug 1998, (e) 13 Aug 1998, and (f) 1 Feb 1999.

other manifestation of NUBF is strong horizontal reflectivity gradients across EDOP and PR footprints. This is the case for Fig. 9d in which the flight line crosses a strong gradient region of reflectivity. The TRMM footprint is relatively large and hence may sample this region differently than EDOP and S-POL.

For small or rapidly evolving storms, a good temporal match is essential for validation. Figure 9e shows the

TABLE 3. Events with quasi-coincident TRMM–EDOP observations. (Times are in UTC.) The EDOP times are the start/end of a straight-and-level flight leg. The TRMM overpass time over the domains shown in Fig. 2 may take 10–30 s, but the time closest to the PR coverage of the feature of interest is shown. The ground-based radar time is the start time of a volume scan. KLTX is the Wilmington, NC, WSR-88D radar.

Date	Type of event	EDOP	TRMM	Ground radar
21 Apr 1998	Frontal–mostly stratiform	0624–0645	0633:45	KFWS 0636:46
13 Aug 1998	Decaying convective cell	2225–2230	2229:52	S-POL 2225:06
26 Aug 1998	Hurricane Bonnie (pass 1)	1141–1213	1137:16	KLTX 1136:10
26 Aug 1998	Hurricane Bonnie (pass 3)	1447–1512	1450:30	KLTX 1455:03
1 Feb 1999	Growing convective cell	1817–1821	1825:47	S-POL 1816:00
23 Feb 1999	Small MCS	2056–2103	2100:47	TOGA 2100:19

collapse of the trailing part of central Florida convection evidenced by the rapid reflectivity decrease between 4- and 8-km altitude from 2219 and 2231 UTC. The discrepancies in the hurricane cases (Fig. 9b) are largely due to nonsimultaneity; in this case advection mentioned earlier is likely the cause of some of the differences. The best time coincidence for the cases presented is the small MCS on 23 February 1999 (Fig. 9c). The reflectivity profile differences for this case are largely due to calibration differences, PR attenuation correction, and NUBF algorithms. Clearly in this latter case, the PR profile nicely matches the S-POL, TOGA, and EDOP traces.

5. Summary and conclusions

In this paper we compare horizontal and mainly vertical reflectivity structures from the TRMM PR 2A23 and 2A25 product to data from higher resolution, more sensitive radars, both airborne (i.e., EDOP) and ground-based. In the comparison, ground radar and PR data are interpolated to a horizontal grid, as well as to the geolocated cross sections covered by EDOP beams. This exercise is not trivial because of different beam geometries, resolutions, earth references, and the ER-2 aircraft motions, but it is essential for the validity of point-to-point comparisons. Both the PR and EDOP view precipitating systems from (near) zenith, yet there are several significant differences, the most important one being the horizontal resolution.

This study compares the shapes of the reflectivity profiles, and their dependence on storm size and type. The comparisons yield highly favorable agreement of the PR with EDOP and the ground radars for large precipitation regions. It is known that a significant portion of the rainfall results from convection smaller than the PR footprint, and that PR reflectivity profiles and rain-rate estimates depend on storm size. In fact a correction for NUBF is applied operationally in obtaining the 2A25 product. Simple calculations in this paper show that the PR-measured reflectivity, and hence rain rate, become increasingly reduced, not only as the storm cell size decreases, but also as the cell is displaced farther from the PR beam center. The effects of beam filtering and limited sensitivity compound to make small and/or weak cells entirely or partly undetectable by the PR, and to render PR statistics of derived variables such as storm-top height and rain type unreliable for small systems. A bias is also possible for larger (convective) systems since high reflectivity gradients typically occur along convective storm edges. The PR would measure an artificial stratiform fringe around these high-gradient regions. Therefore, the stratiform fraction may be overestimated, especially over tropical landmasses where convective cores tend to be smaller and stronger, and where the convective fraction of the total precipitation is larger [$\sim$60%–70% over land vs $\sim$50%–60% over the tropical oceans, Houze (1997)]. In particular users of level-3 (monthly mean) TRMM PR products should be aware of the strong scale dependency of PR estimates. For instance, Tao et al. (2000) find that the PR-based estimation of the stratiform rain fraction over land is significantly larger (15% on average) than the TMI-based estimation, for February 1998. Over the ocean the two algorithms give very similar estimates, on average. At level 3, the scale dependency is impossible to assess because spatial information of individual storms is lost in the processing from instantaneous to mean rain rates.

It is a rare event when a TRMM overflight is within a few minutes of a straight-and-level ER-2 flight leg, a ground-based radar volume scan, and a precipitating system of interest. In fact the differences in presented reflectivity cross sections derived from the various radars are largely due to nonsimultaneous sampling (allowing significant advection and evolution). Six cases from TEFLUN (A and B), CAMEX-3, and TRMM LBA were sufficiently simultaneous and data rich for radar intercomparisons. These cases represent various meteorological situations: a broad, mostly stratiform rainband; a hurricane; a small MCS; a dissipating convective storm; and a small yet active convective cell. Some preliminary conclusions can be drawn from this small sample of EDOP–TRMM coincidences.

- High-resolution EDOP reflectivity sections show that the TRMM PR, given its resolution and sensitivity threshold, captures most of the spectrum of sizes and intensities of precipitating systems very well, in terms of both 2A25 vertical reflectivity structure and deduced variables.
- The PR accurately detects bright bands, their depth and their height; in fact in this regard it outperforms WSR-88D radars at typical operating ranges. High-resolution vertical reflectivity profiles from EDOP suggest that the PR rainfall classification is realistic, even at high incidence angles.
- EDOP reflectivities can be degraded to provide a TRMM PR surrogate for simulation/retrieval studies. Therefore, EDOP and AMPR data can be used as PR/TMI substitutes for ER-2 flights aimed at a specific storm and its life cycle.
- The vertical structure, intensity, and rainfall classification of convective cells smaller than the PR footprint may be erroneous. For relatively small cells that are common in the Tropics, underestimation of reflectivity and storm-top heights can result in misclassification of convective precipitation as stratiform.
- The limited PR sensitivity results in the failure to detect very weak precipitating systems and small convective cells; storm-top heights are also underestimated, especially in tropical stratiform regions where reflectivity profiles fall off rapidly with height. This may not have direct ramifications on latent heat release, but it will have implications on radiative heating and cooling and general model validation.

Further work is aimed at a more detailed comparison and evaluation of TRMM products, including attenuation and surface backscatter cross section, as well as microwave radiances.

Acknowledgments. This work was supported under TRMM Science Team funding provided by NASA Headquarters TRMM Program Scientist Dr. Ramesh Kakar. Several key people in field campaign operations deserve special credit such as Dr. Ed Zipser, Ms. Robbie Hood, Dr. Steve Rutledge, and Walt Peterson. Dr. Vivekanadan, Dr. Ed Brandes, and others were key in the S-POL radar science direction during ER-2 flights. Dr. Steve Bidwell and Mr. Ed Zenker are greatly appreciated for the superb engineering effort on the EDOP instrument. We are appreciative to Dr. Bob Meneghini for many excellent science discussions, and to Mr. Carlos Morales and Dr. Liang for guidance on reading PR and other TRMM datasets. Radar data and assistance were provided by Mr. Dave Wolff (TOGA) and Mr. Bob Rilling at NCAR (S-POL). Many others answered questions that arose due to the diverse nature of the datasets used in this paper.

APPENDIX A

Mapping Algorithms

a. EDOP coordinates and mapping

An accurate interpolation of all the radar datasets into a common (earth relative) coordinate system is essential before the various datasets can be compared. The coordinates of the EDOP flight line images are chosen as this common frame of reference. The ER-2 tracks presented in this paper are relatively linear although occasionally there are small aircraft heading adjustments (such as pass 1 on 26 August 1998, Fig. 2c) or other more minor deviations in heading due to crosswind variations at altitude. In order to retain accuracy in the mapping of other datasets, each beam of EDOP data (~100-m intervals along the flight track) is assumed to be normal to the earth's surface and each gate (37.5-m intervals) has an associated earth location (δ, α, z) = (latitude, longitude, height above the earth's surface). This is a reasonable assumption since the ER-2 is relatively stable during flight with roll excursions of $< \pm 0.25^\circ$ (i.e., ± 175 m on the ground) and pitch excursions $< \pm 1^\circ$. The (δ, α, z) coordinates of gates in each beam are then gridded such that pixels in a single vertical column represent a single dwell of data, and the x axis represents dwells along the flight line. In all cases presented here, the difference between ground-relative height (for EDOP and ground radar data) and mean sea level height (for PR data) is ignored because all of the regions studied were less than approximately 400 m above sea level.

b. Ground-based radar mapping

Ground-based radar data are three-dimensional and therefore a mapping onto a level, uniformly gridded plane or to EDOP vertical sections [appendix A(a)] is required. Two approaches were examined for mapping ground-based radar data, each of which has merits. The first approach is to degrade all the datasets to the lowest common resolution volume. This volume has the horizontal dimensions of the PR footprint and the range-dependent vertical depth of the beam of the nearest ground radar. This allows for examination of differences between datasets all on the same, lowest-resolution scale. This approach is ideally suited for calibration comparisons but it does not deal with the NUBF problem. The second approach is to interpolate all the observations to the coordinates of the highest-resolution data (i.e., EDOP), in order to examine the ability of lower-resolution data to capture the ''true'' reflectivity structure. The second approach is used in this paper, that is, PR and ground-based radar reflectivities are resampled to a dense grid representing the beam and gate spacings of nadir EDOP data. One exception is the PR's vertical resolution, which is maintained at its nadir value (250 m).

Ground-based radar data collected in spherical coordinates (r, ϑ, ϕ) = (range, azimuth, elevation) are mapped to EDOP vertical sections using the transformation approximations developed in Heymsfield et al. (1983). These ''small-range'' equations are applicable to distances less than about 200 km from the radar and can be summarized as follows:

$$s = \frac{r\cos\phi}{[1 + (r/R')]\sin\phi} \tag{A1}$$

$$x = s\frac{R}{R'}\sin(\theta) \tag{A2}$$

$$y = s\frac{R}{R'}\cos(\theta) \tag{A3}$$

$$\alpha = \alpha_s + \frac{x}{R\cos\delta} \tag{A4}$$

$$\delta = \delta_s + \frac{y}{R} - \frac{x^2}{2R^2}\tan\delta_s, \tag{A5}$$

where R is the earth local radius at the radar station, the effective earth radius $R' = 4R/3$, (x, y) is the radar-relative horizontal location, and subscript s refers to the radar location; z is obtained from the standard $4R/3$ correction. These approximations provide (δ, α, z) to within a few tenths of a kilometer at 200 km from a radar.

Using the above equations, each EDOP pixel has an associated (r, ϑ, ϕ) location. At a given pixel, a search is performed over the radar volume scan for the eight surrounding range gates (four each from the elevation scans above and below ϕ). Interpolations are performed

using trilinear interpolation, that is, first the reflectivities are interpolated bilinearly to (r, ϑ) on each elevation scan, and then these values are linearly interpolated between adjacent scans in ϕ. To avoid averaging biases, averaging is performed on linear rather than logarithmic reflectivity values. While better interpolation schemes with better performance can be utilized, the linear interpolation, also used in Heymsfield et al. (1983), is simple to implement and provides reasonable results. Trapp and Doswell (1999) address the ramifications of using bilinear versus Cressman and Barnes interpolation; the latter two have more easily understandable filtering responses.

The ground-based radar PPI scans shown in Fig. 2 are constructed using an almost identical interpolation approach to the above and in Heymsfield et al. (1983). This approach uses Eqs. (A1)–(A5) and interpolation to a regular latitude–longitude grid with intervals of 0.01° in latitude and longitude.

c. TRMM PR mapping

For both CAPPIs and cross sections, the PR 2A25 profiles are assumed vertically oriented even though they can be tilted up to ~17° scan angle. This implies that an elevated echo (15 km high) at the edge of the PR swath would be displaced about 4 km (i.e., one PR pixel spacing) horizontally from the surface position of the profile, toward the TRMM nadir position. In most cases, this is not a problem since the PR scan angles are usually smaller and the echo heights are less than 10 km.

For each range gate in an EDOP profile with an (δ, α, z) coordinate, a search is performed on the TRMM data for the four profiles surrounding this (δ, α) location. Then Cressman weighting (Cressman 1959) is applied to these four profiles, level by level in the PR profile, at 250-m intervals. The weighting function is given by

$$Z_{\text{edop}} = \sum_{i=1}^{4} \frac{\kappa^2 - d^2}{\kappa^2 + d^2} Z_{\text{PR}}, \qquad \text{(A6)}$$

where $\kappa = 5.0$ km is the influence radius; d is the distance from the EDOP pixel location ($d < \kappa$); and Z_{edop} and Z_{PR} are the interpolated and original PR reflectivities, respectively. This function captures most of the PR features well in the interpolated vertical sections and performed slightly better than bilinear interpolation and significantly better than taking the PR gate nearest the EDOP gate (i.e., ''nearest neighbor''). The radius of influence was chosen as the minimum value for which at least four PR pixels were within κ. The Cressman filter results in minimal smoothing of the data.

The constant-altitude PR echo maps shown in Fig. 2 are constructed using a standard Delaunay triangulation scheme to map irregular gridded points to a regular latitude–longitude grid with a grid mapping interval of 0.02° in latitude and longitude.

d. Mapping of two-dimensional TRMM parameters

Many of the TRMM parameters are located only by their latitude and longitude, not by their altitude, for instance the TMI 2B11 brightness temperatures. Some of these variables do have a physical altitude, for example, infrared temperatures are representative of the cloud top. Lateral displacements due to off-nadir TRMM-scanning angles are ignored, even for the TMI that scans at a constant 53°. These quantities are interpolated to the EDOP profiles in an identical fashion to the PR data, as described in appendix section A(C), using a Cressman weighting [Eq. (A6)]. The exception to this are discrete variables such as the rain type (2A23). For such quantities no interpolation can be performed and the TRMM pixel nearest the EDOP profile is used.

APPENDIX B

Simulating PR Reflectivities Using EDOP Data

a. Technique and limitations

The simulation of spaceborne data using airborne radar data has been discussed by Amayenc et al. (1996) and Durden et al. (1998), and a similar technique is used here. It is well known that the radar antenna main- and sidelobes cause distortion of a meteorological target (e.g., Donaldson 1964). This is particularly true in sharp hydrometeor gradient regions as commonly found at the edges of deep convection. A more significant problem is the NUBF problems mentioned in section 2a. Both of these problems can cause a significant misrepresentation of the reflectivity. For simplicity, the filtering effects of a radar beam can be calculated in the following manner. Let the two-way illumination function be

$$I_*^2 = \frac{4 \ln 4}{\pi b^2} \exp\left[-\left(\frac{x^2}{b^2} + \frac{y^2}{b^2}\right)\right], \qquad \text{(B1)}$$

where I_*^2 is the normalized two-way antenna illumination function for a circular beam (e.g., Donaldson 1964). Clearly, this is a Gaussian distribution function, with width b, and distances x and y relative to the beam center. The coefficient in front of the exponential is the normalizing factor. The two-way illumination function falls one-quarter of its maximum value at $(x^2 + y^2)^{1/2} = b$. In the case of the PR, $2b = 4.3$ km. Sidelobe effects are ignored for this simplistic representation. Because EDOP data are only 1D (along track), the EDOP simulation of the PR involves a convolution of the data with a Gaussian weighting function [similar to Eq. (B1) with $y = 0$]. Last, a reflectivity threshold is applied, reflecting the limited sensitivity of the PR. Differences in frequency between the PR and EDOP lead to differences in attenuation. It is assumed that the PR attenuation correction (Iguchi and Meneghini 1994) is accurate and that EDOP reflectivities are not significantly attenuated; in other words, no further attenuation cor-

rection is performed in the simulation process. Also, the effect of decreasing vertical resolution of the PR with increasing scanning angle is ignored, and the degraded EDOP data have a 250-m vertical resolution independent of incidence angle.

There are limitations when using EDOP reflectivities for simulating PR data. A perfectly ''degraded'' EDOP section will normally not perfectly match the corresponding PR section for two reasons: lack of high-resolution information about the third dimension (i.e., across the flight track of the ER-2), and nonsimultaneity of the observations. Simultaneous records will compare poorly when reflectivity contours (on a map) are tightly packed along an ER-2 flight leg, that is, when the ER-2 flies along precipitation systems, rather than across them. The radar maps in Fig. 2, as well as passive visible, infrared, and microwave data from scanning instruments on the ER-2 can be used to assess cross-track variability. Nonsimultaneity is often a more serious problem; for instance, it takes the ER-2 about 8 min to sample a 100-km-long storm, while it takes the TRMM satellite about 14 s to travel the same distance (Table 2). Poor comparisons can be expected from rapidly evolving storms and when a high-reflectivity gradient is advected across an ER-2 flight leg. Small thunderstorms are especially difficult to compare because of NUBF and because they are typically short-lived. For larger (stratiform) systems a larger time lag between EDOP and the PR is acceptable.

b. Effects of cell locations on EDOP simulations of the PR

Location of the averaging interval [i.e., the antenna beam function (B1)] relative to cells smaller than the PR footprint, has a significant effect on the EDOP simulations of the PR and the measured PR reflectivities. This can be shown quantitatively beginning with (B1). For mathematical convenience the storm reflectivity is represented by

$$\zeta(x, y) = Z_o \exp\left[-\left(\frac{x^2}{r_c^2} + \frac{y^2}{r_c^2}\right) \ln 2\right]. \qquad \text{(B2)}$$

The storm is Gaussian and has a width r_c in the x and y directions and a peak value of Z_o. The reflectivity measured with a finite beamwidth is given by

$$Z_m(X, Y) = \int_{-\infty}^{\infty} \int_{-\infty}^{\infty} \zeta(x, y) I_*^2(x - X, y - Y)\, dx\, dy, \qquad \text{(B3)}$$

where (X, Y) is the location of the beam center relative to the storm cell. After integration of (B3) is performed using (B1)–(B2), Z_m can be given as

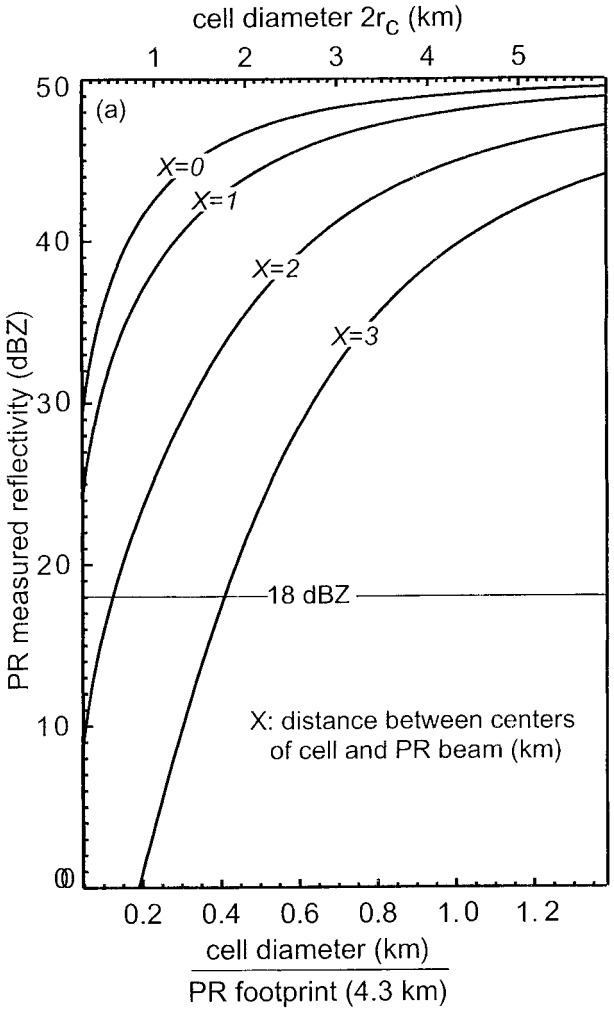

FIG. B1. Scale dependency of PR reflectivity estimates. The curves show the variation of PR-measured reflectivity as a function of the storm cell size, for various cell locations relative to the center of the PR footprint. The horizontal shape of the storm cell is assumed to be bell-shaped with a maximum reflectivity of 50 dBZ. The PR beam illumination function is also assumed to be Gaussian.

$$Z_m(X, Y) = Z_{mo} \exp\left\{-\ln 2\left[\frac{X^2}{\left(\frac{b^2}{2} + r_c^2\right)} + \frac{Y^2}{\left(\frac{b^2}{2} + r_c^2\right)}\right]\right\}$$

$$Z_{mo} = Z_o\left(1 + \frac{b^2}{r_c^2/2}\right)^{-1}. \qquad \text{(B4)}$$

Thus the beam-averaged storm is also Gaussian, but with its maximum reflectivity reduced to Z_{mo}, and its width in the x and y directions increased from r_c to $(b^2/2 + r_c^2)^{1/2}$. Here Z_{mo} provides information on the decrease of PR-measured reflectivity with distance of the cell from the PR footprint's center, where this distance is expressed relative to the cell size, that is, b/r_c. For the case of a very narrow beam (i.e., $b \ll r_c$), then the

measured reflectivity reproduces the true reflectivity and (B4) reverts to (B2). When the beam is broad relative to the size of the cell (i.e., $b \gg r_c$), then $Z_{mo} < Z_o$, and the true reflectivity distribution is broadened.

The variation of the PR-measured reflectivity Z_m with cell size and location relative to the beam's center is shown in Fig. B1. Four cases range from when the cell is centered on the antenna illumination function ($X = 0$), to when the cell is far off it ($X = 3$ km, which is just below the maximum distance between a cell and the nearest PR beam center). When the cell is larger than the PR footprint, the PR reflectivity approaches $z_o = 50$ dBZ. The PR reflectivity decreases faster than linearly with decreasing cell size, as well as with increasing distance between the cell and the PR beam center. For a large cell of 4.3-km diameter, the PR-measured reflectivity ranges from about 49 dBZ for the cell centered on the illumination function ($X = 0$) to 39 dBZ when it is far off center ($X = 3$ km). For a medium-size (2-km diameter) cell, the reflectivities range from 47 dBZ ($X = 0$ km) to 21 dBZ ($X = 3$ km). The latter is very close to the PR noise floor. Of course, if the cell is on the edge of one PR beam, the adjacent PR beam will measure a similar reflectivity from the same cell; that is, the cell is broadened.

In summary, storm cells and borders that are small relative to the PR footprint are broadened. If the median convective cell size is 1.9 km, as is the case for summer storms near the mid-Atlantic coast (Goldhirsh and Musiani 1986), and if the distance between the centers of the cell and the beam is 1.5 km [i.e., the mean or most likely distance, $4.3/(2\sqrt{2})$], then the PR reflectivity is reduced about 11 dBZ from the peak cell reflectivity. The reflectivity deficit is larger for smaller cells and those off-center relative to the PR beam. The combination of filtering and limited sensitivity may cause weak cells, or the upper portion of stronger cells, to remain undetected by the PR. Storms larger than the PR footprint tend to be surrounded by an artificial weak-echo fringe.

REFERENCES

Amayenc, P. M., J. P. Diguet, M. Marzoug, and T. Tani, 1996: A class of single- and dual-frequency algorithms for rain-rate profiling from a spaceborne radar. Part II: Tests from airborne radar measurements. *J. Atmos. Oceanic Technol.,* **13,** 142–164.

Biggerstaff, M. I., and S. A. Listemaa, 2000: An improved scheme for convective/stratiform echo classification using radar reflectivity. *J. Appl. Meteor.*, **39,** 2129–2150.

Bolen, S. M., and V. Chandrasekar, 1999: Comparison of satellite-based and ground-based radar observations of precipitation. Preprints, *29th Conf. on Radar Meteorology,* Montreal, PQ, Canada, Amer. Meteor. Soc., 751–753.

Cressman, G. P., 1959: An operational objective analysis system. *Mon. Wea. Rev.,* **87,** 367–374.

Datta, S., B. Roy, L. Jones, T. Kasparis, P. S. Ray, Z. Ding, and D. Charalampidis, 1999: Evaluation of TRMM precipitation radar rainfall estimates using NEXRAD and rain gauges in Central and South Florida. Preprints, *29th Conf. on Radar Meteorology,* Montreal, PQ, Canada, Amer. Meteor. Soc., 754–757.

Donaldson, R. J., Jr., 1964: A demonstration of antenna beam errors in radar reflectivity patterns. *J. Appl. Meteor.*, **3,** 611–623.

Durden, S. L., Z. S. Haddad, A. Kitiyakara, and F. K. Li, 1998: Effects of nonuniform beam filling on rainfall retrieval for the TRMM precipitation radar. *J. Atmos. Oceanic Technol.*, **15,** 635–646.

Goldhirsh, J., and B. Musiani, 1986: Rain cell size characteristics derived from radar observations at Wallops Island, Virginia. *IEEE. Trans. Geosci. Remote Sens.,* **GE-24,** 947–954.

Heymsfield, G. M., K. K. Ghosh, and L. C. Chen, 1983: An interactive system for compositing digital radar and satellite data. *J. Climate Appl. Meteor.*, **22,** 705–713.

——, and Coauthors, 1996a: The EDOP radar system on the high-altitude NASA ER-2 aircraft. *J. Atmos. Oceanic Technol.,* **13,** 795–809.

——, I. J. Caylor, J. M. Shepherd, W. S. Olson, S. W. Bidwell, W. C. Boncyk, and S. Ameen, 1996b: Structure of Florida thunderstorms using high-altitude aircraft radiometer and radar observations. *J. Appl. Meteor.,* **35,** 1736–1762.

——, J. B. Halverson, and I. J. Caylor, 1999: A wintertime Gulf Coast squall line observed by EDOP airborne Doppler radar. *Mon. Wea. Rev.,* **127,** 2928–2949.

Hitschfeld, W., and J. Bordan, 1954: Errors inherent in the radar measurement of rainfall at attenuating wavelengths. *J. Atmos. Sci.,* **11,** 58–67.

Houze, R. A., Jr., 1989: Observed structure of mesoscale convective systems and implications for large-scale heating. *Quart. J. Roy. Meteor. Soc.*, **115,** 425–461.

——, 1997: Stratiform precipitation in regions of convection: A meteorological paradox? *Bull. Amer. Meteor. Soc.*, **78,** 2179–2196.

Iguchi, T., and R. Meneghini, 1994: Intercomparison of single-frequency methods for retrieving a vertical rain profile from airborne or spaceborne radar data. *J. Atmos. Oceanic Technol.,* **11,** 1507–1516.

——, T. Kozu, R. Meneghini, J. Awaka, and K. Okamoto, 2000: Rain-profiling algorithm for the TRMM precipitation radar. *J. Appl. Meteor.*, **39,** 2038–2052.

Johnson, R. H., and G. S. Young, 1983: Heat and moisture budgets of tropical mesoscale anvil cloud. *J. Atmos. Sci.,* **40,** 2138–2147.

Kozu, T., and T. Iguchi, 1999: Nonuniform beamfilling correction for spaceborne radar rainfall measurement: Implications from TOGA COARE radar data analysis. *J. Atmos. Oceanic Technol.,* **16,** 1722–1735.

Kummerow, C., W. Barnes, T. Kozu, J. Shiue, and J. Simpson, 1998: The Tropical Rainfall Measuring Mission (TRMM) sensor package. *J. Atmos. Oceanic Technol.,* **15,** 809–817.

——, and Coauthors, 2000: The status of the Tropical Rainfall Measuring Mission (TRMM) after two years in orbit. *J. Appl. Meteor.,* **39,** 1965–1982.

McGaughey, G., E. J. Zipser, R. W. Spencer, and R. E. Hood, 1996: High-resolution passive microwave observations of convective systems over the tropical Pacific Ocean. *J. Appl. Meteor.,* **35,** 1921–1947.

Nakamura, K., 1991: Biases of rain retrieval algorithms for spaceborne radar caused by nonuniformity of rain. *J. Atmos. Oceanic Technol.,* **8,** 363–373.

NASDA, 1999: TRMM PR Algorithm Instruction Manual V1.0. Communications Research Laboratory, 52 pp. [Available from Communications Research Laboratory, 4-2-1 Nukui-kitamachi, Koganei-chi, Tokyo 184, Japan.]

Sauvageot, H., F. Mesnard, and R. S. Tenorio, 1999: The relation between the area-average rain rate and the rain cell size distribution parameters. *J. Atmos. Sci.,* **56,** 57–70.

Spencer, R., and Coauthors, 1994: High-resolution imaging of rain systems with the Advanced Microwave Precipitation Radiometer. *J. Atmos. Oceanic Technol.,* **11,** 849–857.

Steiner, M., R. A. Houze Jr., and S. E. Yuter, 1995: Climatological characterization of three-dimensional storm structure from operational radar and rain gauge data. *J. Appl. Meteor.*, **34,** 1978–2007.

Tao, W.-K., and Coauthors, 2000: Retrieved vertical profiles of latent heat release using TRMM rainfall products for February 1998. *J. Appl. Meteor.,* in press.

Testud, J., P. Amayenc, X. K. Dou, and T. F. Tani, 1996: Tests of rain profiling algorithms for a spaceborne radar using raincell models and real data precipitation fields. *J. Atmos. Oceanic Technol.*, **13,** 426–453.

Trapp, R. J., and C. A. Doswell III, 1999: On the objective analysis of weather radar data. Preprints, *29th Conf. on Radar Meteorology,* Montreal, PQ, Canada, Amer. Meteor. Soc., 248–251.

Yuter, S. E., and R. A. Houze Jr., 1995: Three-dimensional kinematic and microphysical evolution of Florida cumulonimbus. Part II: Frequency distributions of vertical velocity, reflectivity, and differential reflectivity. *Mon. Wea. Rev.,* **123,** 1941–1958.